Delft University of Technology

Concrete-to-concrete interfaces

Interlocking architecture for improved toughness

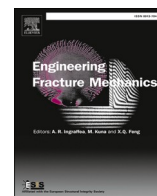Papoulidou, Sofia; He, Shan; Šavija, Branko; Luković, Mladena

Important note
To cite this publication, please use the final published version (if applicable).
Please check the document version above.

Concrete-to-concrete interfaces: Interlocking architecture for improved toughness

Sofia Papoulidou , Shan He , Branko Šavija 🄳, Mladena Luković *

Delft University of Technology, the Netherlands

ABSTRACT

Concrete-to-concrete interfaces are brittle and reinforced with steel to ensure force transfer and provide ductility. Recent research in ceramics and polymers shows that by implementing intricate interlocking geometries, named bistable interlocks, toughness can be added to inherently brittle materials and their connections. In this research, the "bistable interlock" concept is applied to cementitious materials (strain-hardening cementitious composites, SHCC) offering a novel approach to increase the toughness of concrete interfaces. A bistable interlock mechanism is achieved by geometrically designing double-radii surface morphologies that can lock into two hardening positions under tensile loads and is combined with material hardening interlock of SHCC. The investigation focused on the effects of interface shape (straight vs. curved) and geometric characteristics (key length and diameter of interface keys), and interface treatments (as-cast, lubricated, and prefabricated). The findings highlight the critical role of interface treatment. Specimens with an untreated, strong interface were unable to activate bistable behavior, primarily failing due to key rupture. Lubricated interfaces facilitated key pullout, demonstrating in curved specimens up to 80% higher energy absorption compared to untreated specimens. The tensile strength of the architectured interface reached about 30% of the SHCC strength, whereas its deformation capacity was doubled. These results underscore the potential for customized, tough connections and their application in the design of precast concrete components.

1. Introduction

Civil engineering projects often involve constructing various components connected at different stages. Regarding concrete elements (partially or entirely prefabricated), the most common types of concrete-to-concrete connections are *precast-to-precast* and *precast-to-in situ* connections. Although these connections are commonly realized with the help of protruding steel reinforcement to provide ductility and load bearing capacity, for practical and durability reasons it can be beneficial to realize concrete-to-concrete connections without or with reduced amount of reinforcement.

Load transfer in unreinforced concrete-to-concrete interfaces relies on several mechanisms: adhesive bonding, mechanical interlock and friction [1–3]. Factors influencing chemical bonding between concrete layers include moisture exchange [4,5], curing and stress conditions at the interface [6], compatibility of the materials [7], the presence of bonding agents or adhesives [8,9], etc. Surface roughness can increase friction and enhance the bond between two layers of concrete by creating interlocking features between them or by increasing the surface area available for bonding [10,11]. A common practice is to create grooved or chiseled interfaces to avoid

---

delamination of interfaces [12]. Also, other mechanical interlocking features, like shear keys, can increase the shear transfer capacity of a connection [13,14]. Not only the strength, but also the deformational capacity of the interface is critical [15]. Especially when the connection should accommodate large deformations (e.g. differential shrinkage in repair and strengthening systems), increased roughness provides higher fracture energy and deformational capacity of the interface [16,17]. Recent developments in concrete 3d printing also focused on employing (mechanical) interlocking, either for improving interlayer bond strength [18], for modular manufacturing to overcome limitations of the working dimensions of 3d printers [19], or to alleviate anisotropy of 3d printed fiber reinforced materials without introducing additional reinforcement [20].

Mechanical interlocking demonstrates remarkable benefits also in other brittle and quasi brittle materials, by improving damage tolerance, energy absorption, and adaptability [21]. In [22], examples of bioinspired materials with dense architectures, composed of stiff and strong building blocks, arranged to interact through energy-dissipative interfaces, are presented. Architectured ceramic plates, segmented into interlocking blocks, significantly enhanced the energy absorption and impact resistance of the structure compared to monolithic plates which exhibited a brittle failure, localized to specific sections [23]. Similarly, osteomorphic assemblies in [24] use geometrically interlocking blocks to maintain structural integrity under push out load; even when some blocks fail, the assemblies show recoverable stiffness. Sutured geometries, based on mechanical interlock and inspired by natural materials like diatoms and mollusk shells, are designed to exhibit superior toughness and energy absorption [25,26]. Sutured jigsaw-like connection is created by tangentially blending a series of arcs of circles with radii R_1 and R_2 at positions indicated by angles θ_1 and θ_2 (see Fig. 1a). The connection geometry allows the material to switch between two stable positions under uniaxial tension (see Fig. 1b) without visible damage, offering geometric hardening and delaying localization and spreading of deformations over larger volumes. Due to that characteristic, it was named a Bistable interlock connection. Mirkhalaf and Barthelat [26] used Acrylonitrile Butadiene Styrene (ABS) and by fine tuning the architecture of material through 3d printing (Fig. 2a), they demonstrated up to 10 times the toughness of the base polymer. This resulted from a toughening mechanism associated with controlled pullout, nonlinear deformation and energy
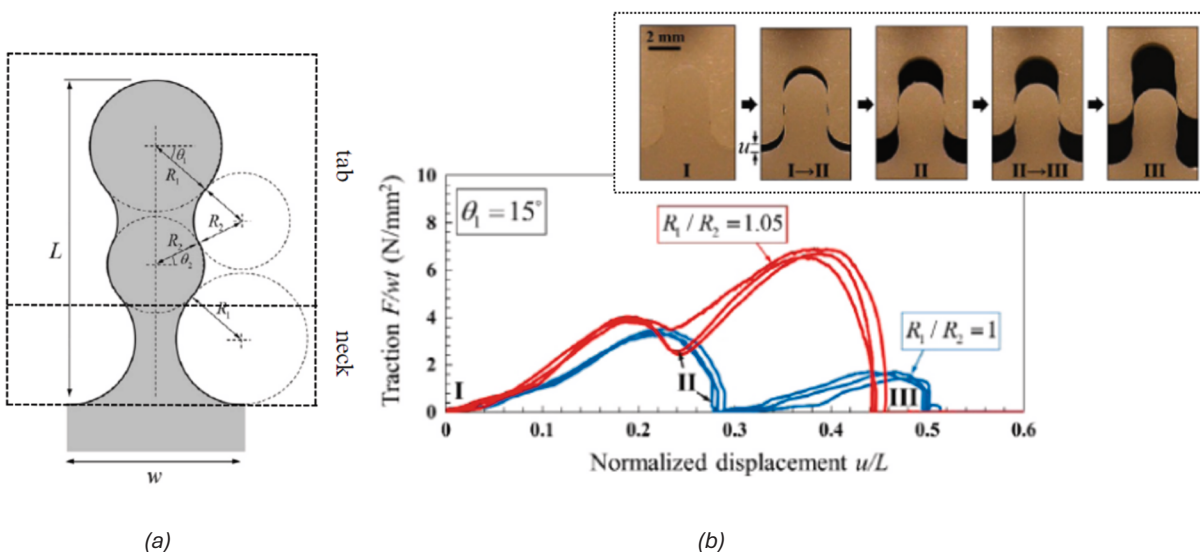
Fig. 1. (a) Overview of bistable interlock tabs and geometry: The key profile consists of arcs of circles or radii R_1 and R_2, and angle θ_1, whereas angle θ_2 is dependent on R_1, R_2 and θ_1; (b) Typical traction-displacement curves of the single bistable interlocked key for radii ratios $R_1/R_2 = 1$ and 1.05 and failure development (Adapted from [26]).

dissipations [6], enabling reversible deformations, enhanced damage tolerance, and re-manufacturability. As the cracks propagated and the tabs opened, several drops in force were observed (Fig. 2b), while the material continued to resist deformation. It must be noted that these systems, which rely on the principle of toughness by segmentation and frictional interfaces, sacrifice some strength and stiffness for increased flexibility and scalability.

This research presents, for the first time, the application of the "bistable interlock" concept to cementitious materials – specifically strain-hardening cementitious composites, SHCC – as a novel method to enhance concrete interface toughness. We hypothesize that concrete-to-concrete interfaces can be *architectured* – that is, designed and fabricated in a way that tailors the connection between the base materials under specific loading conditions. The focus is to increase the ductility of the traditionally brittle concrete-to-concrete interface and investigate the effect of the bistable interlock connection in high-performance cementitious materials. Whereas Mirkhalaf et al. [26] and Malik et al. [25] tested interlocks in brittle materials, in this research a quasi-ductile material – SHCC – is used, potentially offering additional advantages for damage-tolerant connections. This material belongs to the family of fiber-reinforced concrete and is distinguished by its hardening behavior under tension [27], stemming from the fiber-bridging property.

2. Materials and methods

2.1. Specimen design

2.1.1. Specimen overview

Since the focus of this work is the bistable interlock mechanism, specimens were designed with this mechanism as a starting point. Different geometries and interface treatments were used for the bistable interlocked keys. Straight key specimens were designed in a similar way to the bistable interlocked keys as a reference. Straight key geometry has been used in the past e.g., in concrete repair applications [14,16,28,29] and hybrid concrete structures [13,30] and can be used as a benchmark to assess the efficiency of bistable interlocked keys. The overview of all the tested specimens and their geometries is shown in Fig. 3.

2.1.2. Bistable (curved) key specimens

According to Mirkhalaf et al. [26], the radii ratio of the tabs is the governing parameter of the design. They explored different ratios, concluding that $R_1/R_2 \geq 1$ (R_1 and R_2 are defined in Fig. 1a) creates an interlocking phenomenon similar to strain hardening. In the force–displacement diagram (Fig. 2b) the second peak greatly increases with a larger R_1, adding mechanical stability to the system. However, when the R_1/R_2 ratio was higher than a certain limit, the fracture of a key was observed. Herein, we explored 3 different ratios of R_1/R_2: 1.05 (geometry 1), 1.10 (geometry 2), and 1.20 (geometry 3), to understand the role of the specific geometrical interlocking effect and be able to optimize the connection.

To define the magnitude of the radii and the specimen size, two design boundaries have been considered. The first was the "neck" of the key (see Fig. 1a). The neck must be large enough to accommodate the fiber distribution in the key as evenly as possible. Therefore, a neck of around 10 mm was estimated to be sufficient for the fibers used (i.e. 6 mm length). The second one was the dimensions of the test setup used for uniaxial tensile testing. A specimen width of 43 mm ensured that there would be enough bulk material enclosing the key to minimize in-plane bending. Some general design boundaries considered were the width of the specimen and the slope of the dogbone, to create a desirable gauge length without stress concentrations caused by the edges of the clamps while testing. Another important parameter chosen was the interlocking angle θ_1 (see Fig. 1a). By defining the main parameters θ_1, R_1, and R_2, the remaining
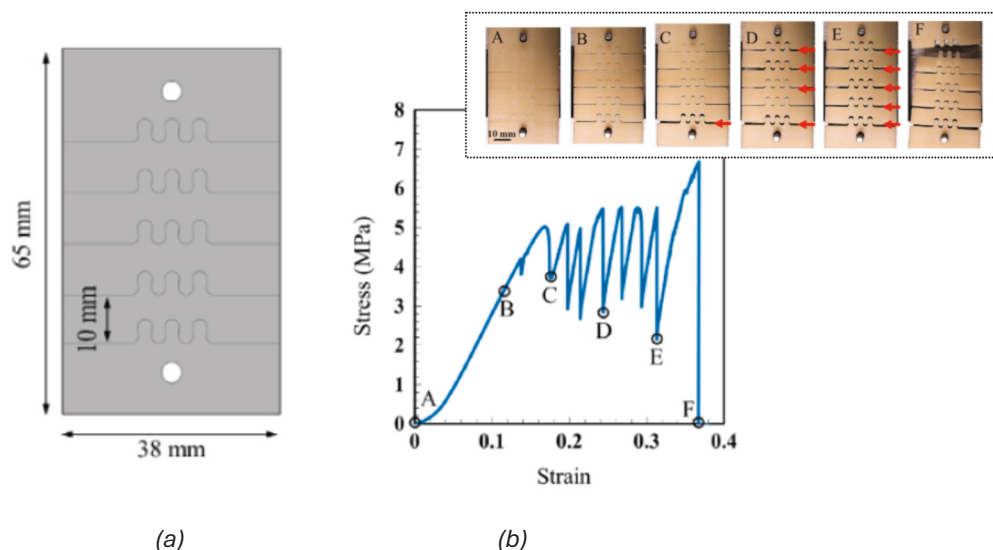

Fig. 2. (a) Overview of the geometry in multilayer interlocked material and) (b) stress–strain curves under monotonic tension (Adapted from [26]).
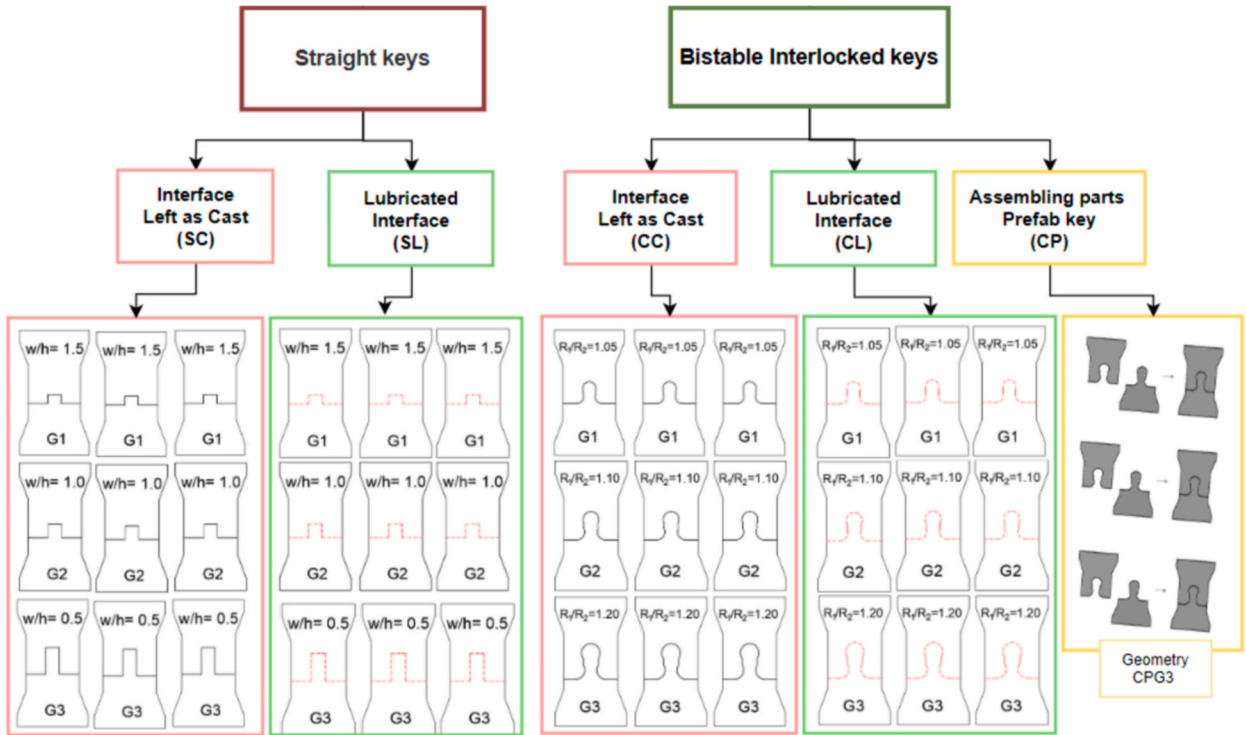
Fig. 3. Categorization and nomenclature of SHCC specimens.

design parameters (θ_2, key length L, key width w) were determined from the geometry. An overview of the chosen parameters for the 3 variations of bistable interlocked keys is given in Table 1.

Furthermore, "prefabricated" bistable interlocked specimens (i.e., a dry connection) were constructed. The tolerance designed between the two parts was 0.5 mm to ensure that the parts fit without stresses during the assembly. This tolerance results in a small R_1/R_2 decrease. Thus, it was judged necessary to choose geometry 3 (Table 1) with the largest radii ratio for these specimens.

2.1.3. Straight key specimens

The parameters of straight key geometries are given in Fig. 4. The width of the keys was 10.80 mm with variable heights according to the w/h ratios indicated in Fig. 4.

2.2. Specimen preparation

To create the dogbone specimens and the designed interface geometry, 3D printing was used (Fig. 5). The printer was a commercial Ultimaker 2; a filament-based 3D printer working with spools of thermoplastic filaments, in this case ABS [20]. The casting was performed in two stages. At first, the molds were prepared with designated auxiliary interface elements to cast the bottom part. After the casting, specimens were vibrated to remove entrapped air, and then they were wrapped with plastic film. The bottom part was left to harden at room temperature for one day. After that, the silicon interface element was removed, and dirt and excessive material were removed from the interface. Then a second stage took place, which involved the casting of the top part. The mixing procedure and proportions used were identical to the previous step. After casting, the specimens were vibrated, wrapped in plastic film, and left at room temperature to harden for one day. The next day, the specimens were demolded and left in a curing chamber (20°C and 98 % relative humidity) for at least 27 more days. In cases where the interface was treated with lubricant, after the hardening of the bottom part and the removal of the silicon top part, an additional step took place. Lubricant (liquid vaseline) was brushed at the interface before casting the top part. After that, the excessive lubricant was wiped out.

For the prefabricated specimens the top and bottom parts were cast simultaneously in their designated molds and then assembled in the out-of-plane direction (Fig. 6).

2.3. Materials

Strain Hardening Cementitious Composite (SHCC) [31,32], a pseudo-ductile fiber-reinforced material with high strain capacity and controlled microcracking under tensile loads, has been used. The SHCC mixture (Table 2) was adapted from the mixture of Zhou et al. [33]. CEM III/B 42.5 N (provided by ENCI, Netherlands) was used as a binder. Finely grinded limestone powder (provided by

Table 1
Design parameters of bistable interlocked (curved) keys.

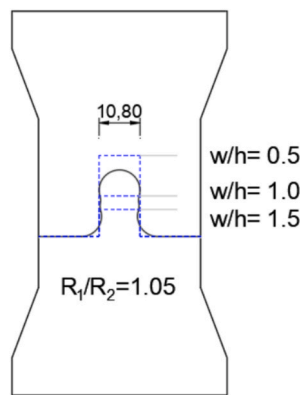| Parameter	$R_1/R_2 = 1.05$ (G1)	$R_1/R_2 = 1.10$ (G2)	$R_1/R_2 = 1.20$ (G3)
Radius R_1 (mm)	5.4	6.21	7.35
Radius R_2 (mm)	5.14	5.65	6.12
Interlocking angle θ_1 (°)	15.0	18.0	26.0
Interlocking angle θ_2 (°)	7.96	3.45	8.46
Key length L (mm) $L = 2[R_1(1 + \sin\theta_1) + R_2(\sin\theta_1 + \sin\theta_2)]$	17.75	20.84	28.34
Key width w (mm) $w = 2(R_1 + R_2)\cos\theta_1$	20.36	22.56	24.21
Smallest key width (mm) for "effective tensile strength"	9.52	10.01	9.5

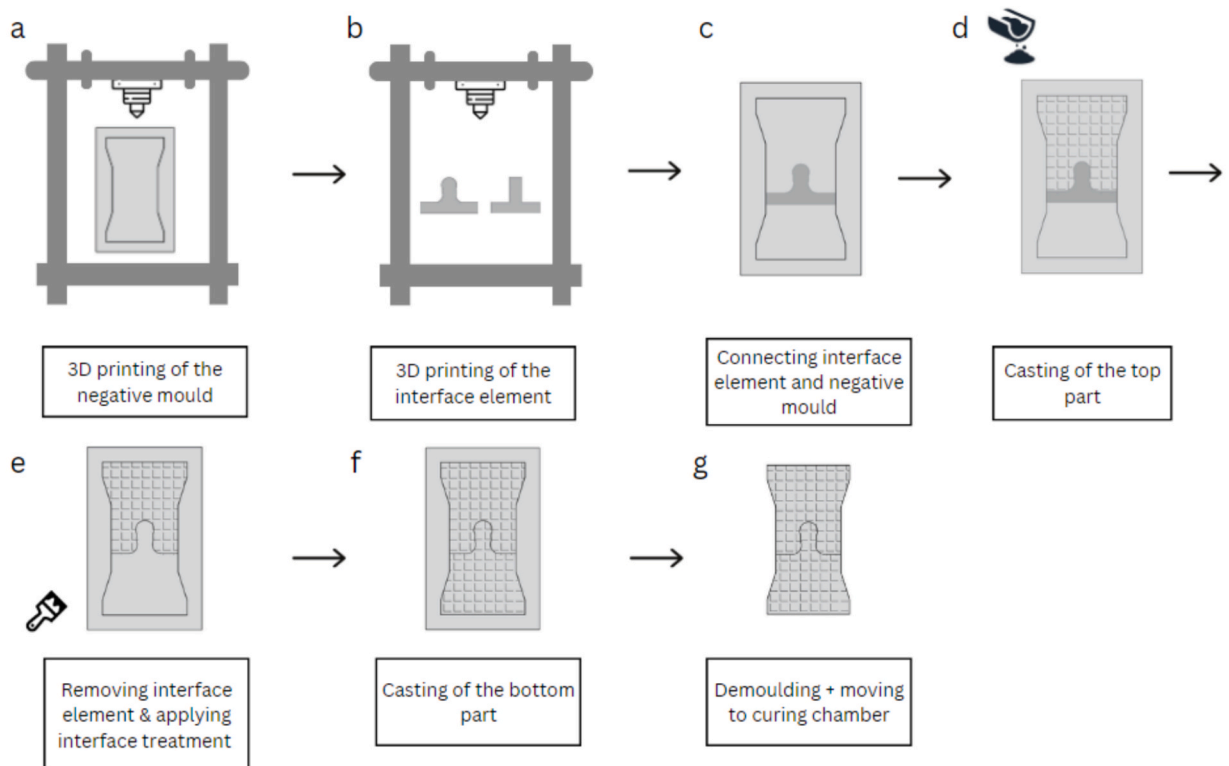**Fig. 4.** Different lengths of straight keys and comparison with bistable geometry of R_1/R_2.

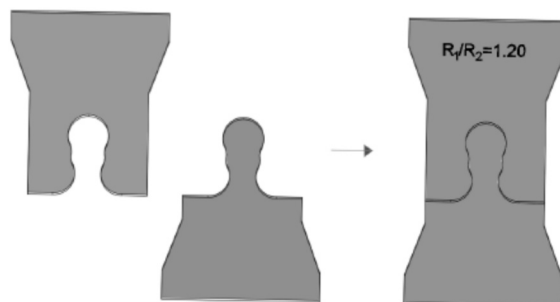**Fig. 5.** Overview of the specimen preparation process.

Fig. 6. Geometry of out-of-plane assembled (prefabricated) specimens.

Table 2
Mixture design of SHCC used in the study.

Ingredient	SHCC
CEM III/B 42.5 N (kg/m^3)	873
Limestone powder (kg/m^3)	873
Water (kg/m^3)	349
Superplasticizer (kg/m^3)	7
Fibers (kg/m^3)	26
by volume (%)	2.6

Calcitec®, Belgium) with a mean particle size of 39 μm (D10: 5.6 μm; D50: 38.2 μm; D90: 70.4 μm) and a particle size distribution similar to that of cement, was used as filler to further reduce the matrix fracture toughness and to facilitate uniform fiber dispersion. In addition, a polycarboxylate-based superplasticizer (MasterGlenium 51, with 35 % solid content by mass) was used to acquire the desired workability. The mixture contained ultra-high molecular weight polyethylene fibers with properties given in Table 3.

The applied fiber volume was 2.6 %. A high fiber volume was chosen to ensure sufficient ductility of SHCC for this connection, to facilitate fiber bridging and allow large deformations of the key. In the future, the fiber volume should be decreased to lower values (e.g. corresponding to commonly used 2 % in SHCC).

Mixing of SHCC consisted of four steps. First, cement and limestone powder were dry mixed in a Hobart mixer at low speed for 5 min. Then, about 60 % of the superplasticizer was mixed with water and added to the dry mixture and mixed until it was homogeneous. Subsequently, fibers were added and mixed for 5 more minutes. Finally, the remaining superplasticizer was added to improve the workability [34].

The compressive strength of SHCC was determined by uniaxial compressive strength tests on 40x40x40 mm^3 cubes, following NEN-EN 196–1 [35]. The loading rate was 0.2 kN/s. In total 18 SHCC specimens were tested at an age of around 90 days.

Uniaxial tensile tests were performed to characterize the strain-hardening capacity of SHCC. Four dogbone SHCC specimens with a cross-section of 13x300 mm^2 were tested in uniaxial tension, also at an age of around 90 days.

Table 3
Properties of ultra-high molecular weight polyethylene fibers used.

Property	
Tensile strength [GPa]	3.0
Young's modulus [GPa]	110
Density [g/cm3]	0.97–0.98
Diameter [μm]	19–43
Length [mm]	6.0
Elongation [%]	2.0–3.0

(a)   *(b)*   *(c)*   *(d)*
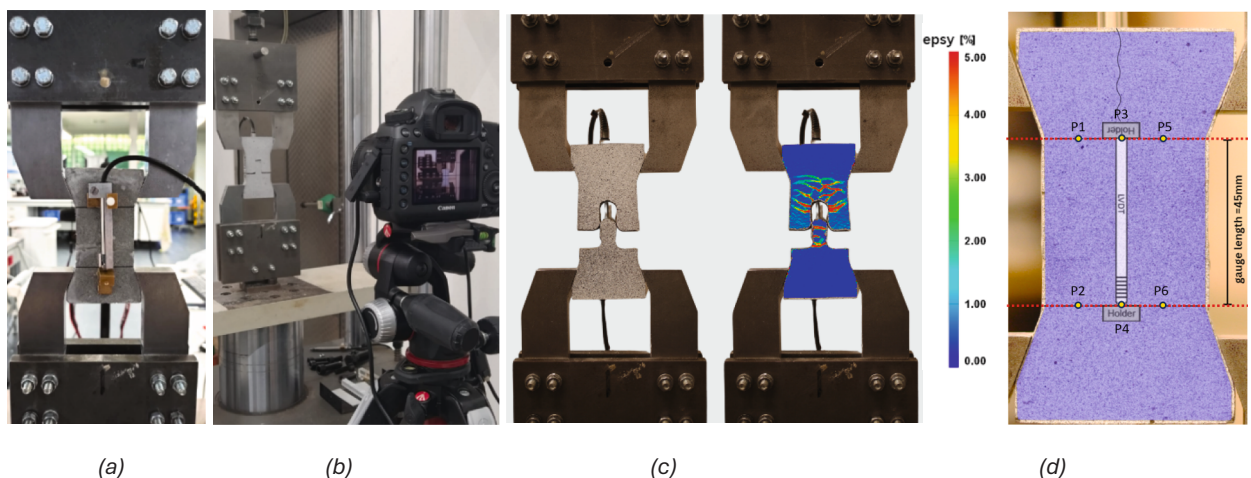
Fig. 7. Direct tensile test and measurement methods (a) LVDT and (b) DIC applied at the opposite sides of the sample (c) stain localization captured by DIC during the pullout test and the legend and (d) DIC and LVDT correlation, with the location of correlation Points in the measurement (P1-P6).
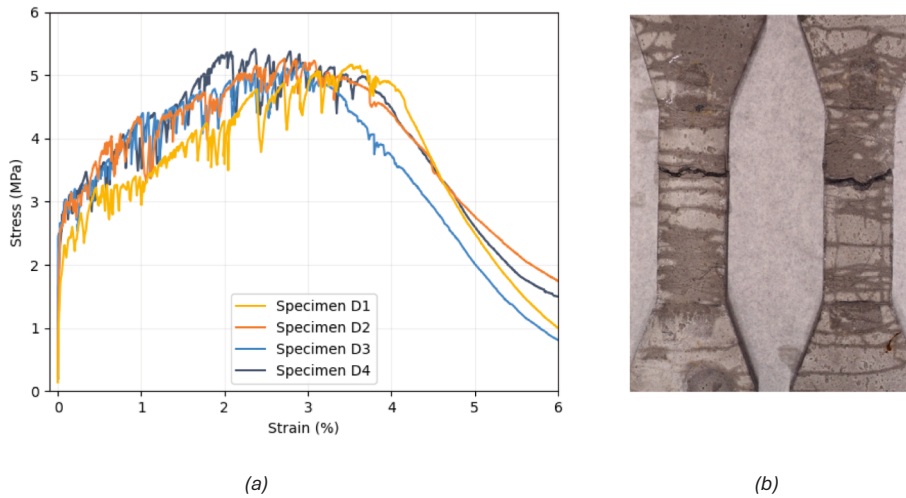
Fig. 8. Tensile test results on SHCC at an age of 90 days (a) stress–strain curves and (b) final crack patterns.

2.4. Tensile tests

Uniaxial tension tests were performed by using a servo-hydraulic testing machine (Instron) under displacement control at a rate of 0.005 mm/s. Regarding the Instron setup, the top clamp could rotate while the bottom was bolted to the testing machine. This enabled alignment and uniform loading of the specimen.

Initially, a pretension of 0.05 kN was applied to the dogbone specimen. During the tests, the deformations were measured by a Linear Variable Differential Transformer (LVDT) fixed on one side of the specimens, with a gauge length of 45 mm for interface tests and 80 mm for SHCC materials tests (Fig. 7a). On the other side of the specimen Digital Image Correlation (DIC) was used (Fig. 7b) to evaluate the displacement field and crack pattern development (Fig. 7c).

DIC is a non-contact optical method that employs tracking and image registration techniques for accurate 2D measurements of changes in images, allowing to calculate deformation, displacement and strain on the observed surface [36,37]. Therefore, deformations were measured simultaneously by LVDTs and DIC (Fig. 7d), with pictures being taken at 10 s interval.

Specimens were loaded until failure. Tests were stopped by releasing the applied load after the tensile load dropped to an approximate value of 0.05kN.

3. Results and discussion

3.1. Material properties

The compressive strength of the SHCC was tested with 3 specimens for each casting batch (6 in total). The average compressive
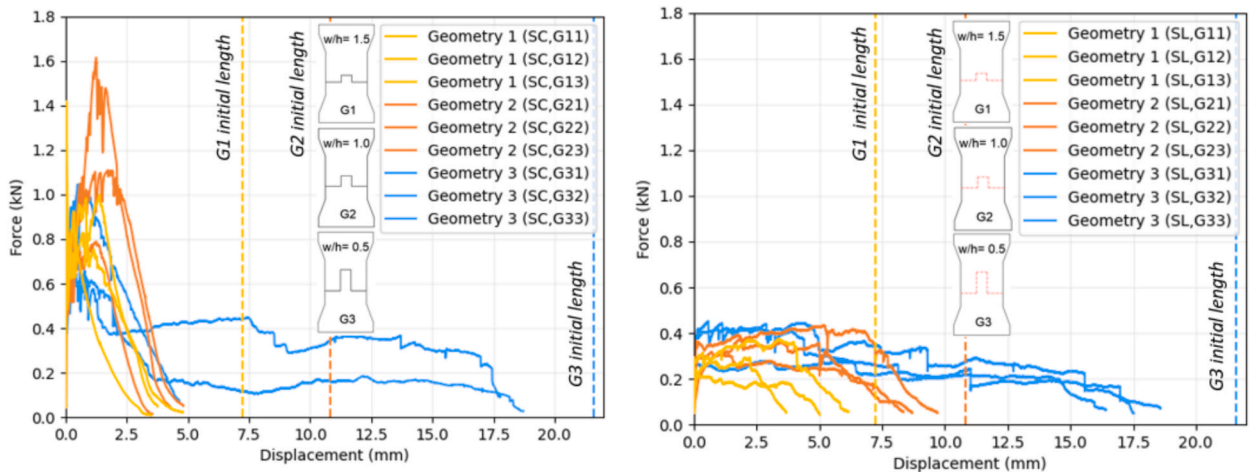

Fig. 9. Force-displacement diagrams for straight key specimens with (a) untreated and (b) lubricated interface.
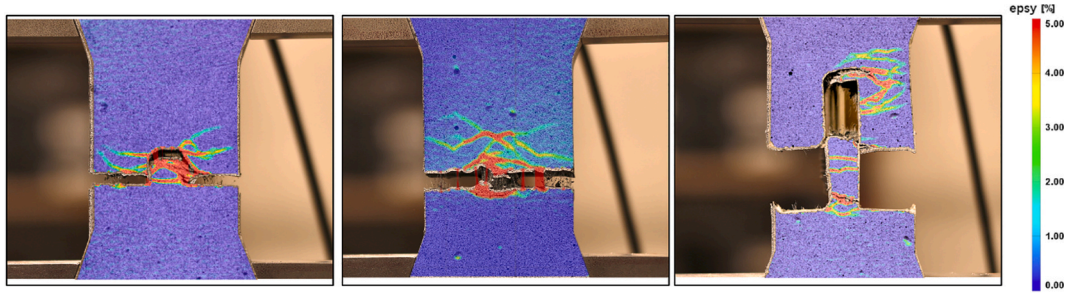
Fig. 10. Failure modes of straight specimens with untreated interface and geometries 1, 2, 3, indicating principal strains in y direction (with the legend).
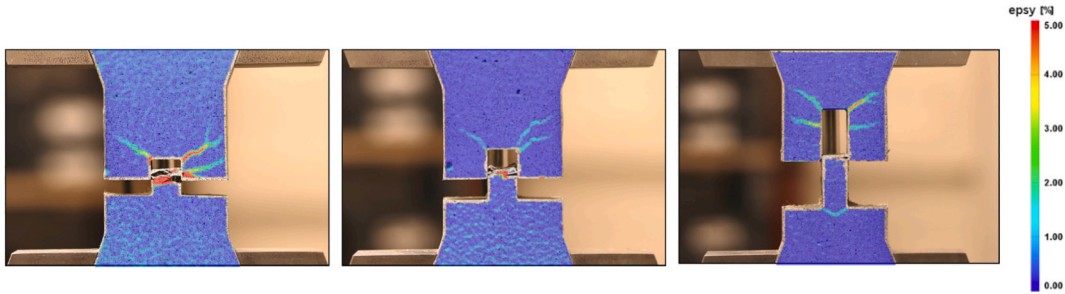

Fig. 11. Failure modes of straight specimens with lubricated interface and geometries 1, 2, 3, indicating principal strains in y direction (with the legend).
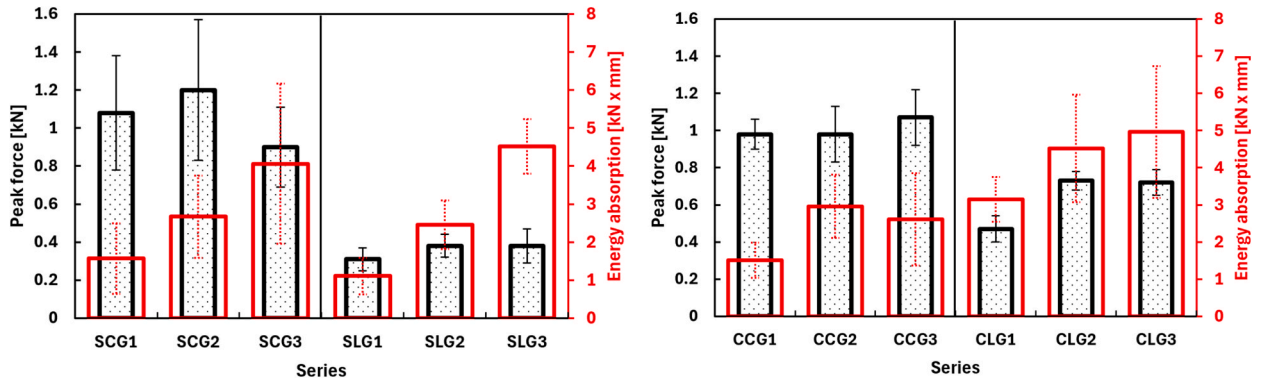

Fig. 12. Peak force and energy absorption for (a) straight and (b) curved specimens.

strength of SHCC was 86.5 MPa with a standard deviation of 8.2 MPa.

Four specimens were tested in uniaxial tension. The first cracking strength was around 2.5 MPa with a coefficient of variation of 5 %. The ultimate tensile strength was 5.3 MPa (Fig. 8a) with a coefficient of variation of 2 %, and multiple cracking observed (Fig. 8b). The strain capacity was 3 % (strain at peak load) with a coefficient of variation of 10 %.

3.2. Influence of the key geometry on the tensile response

A parametric analysis was performed to explore the behavior of interlocking keys subjected to uniaxial tension. The investigated parameters include the geometry/length of the key, the interface treatment method, and the shape (straight or bistable interlocked). The peak force and the energy absorption capacity, calculated as the area under the force–displacement diagram and based on the final measured displacement, were compared for all samples.

3.2.1. Straight key specimens

Specimens with untreated keys resulted in high scatter (Fig. 9a). Most of the specimens resulted in key failure (Fig. 10), although
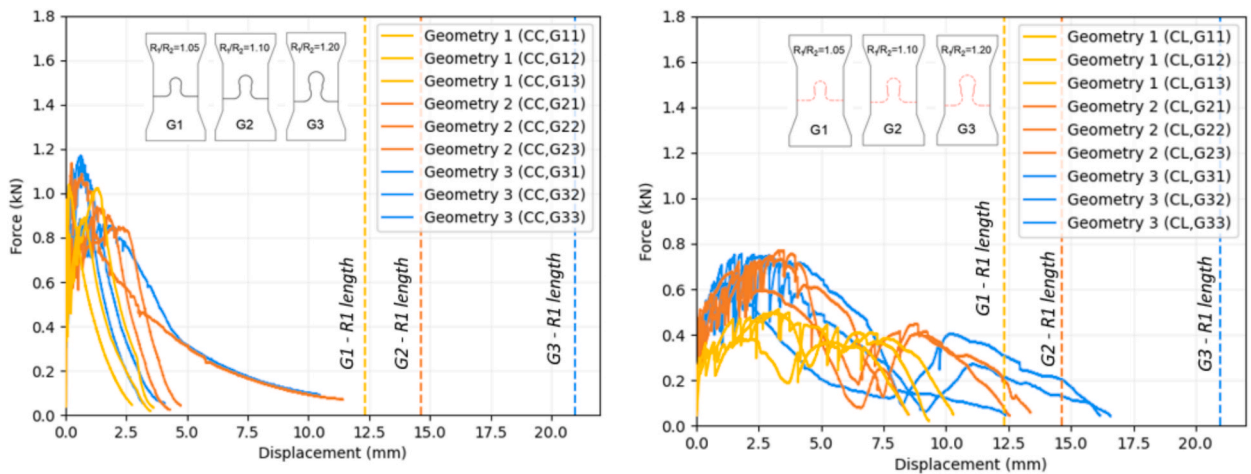
Fig. 13. Force-displacement diagrams for curved key specimens with (a) untreated and (b) lubricated interface.
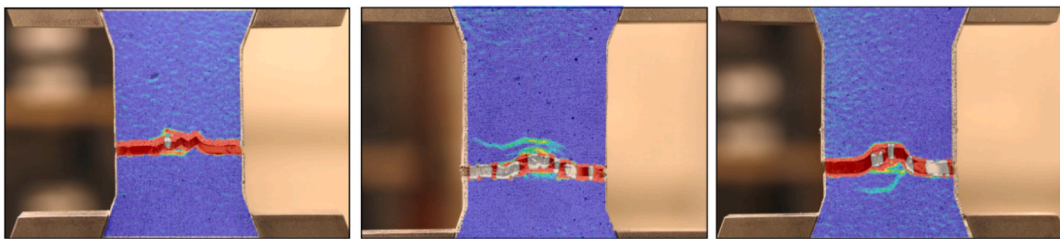

Fig. 14. Failure modes of bistable interlocked specimens with untreated interface and geometries 1, 2, 3 respectively.
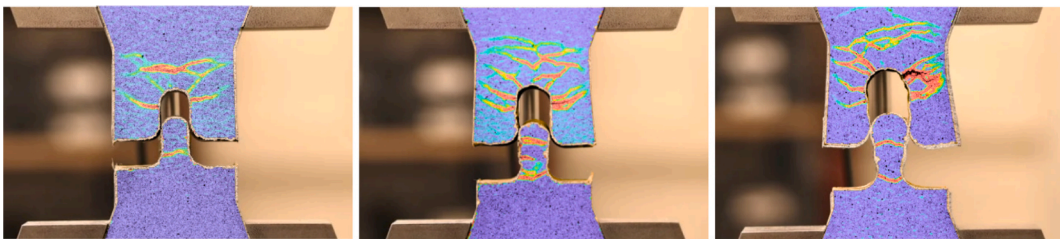

Fig. 15. Failure modes of bistable interlocked specimens with lubricated interface and geometries 1, 2, 3 respectively.

some specimens also exhibited combined pullout and key failure. Only in geometry 2, none of the specimens exhibited pullout, thereby showing the highest capacity on average. It was expected that longer keys would lead to increased frictional resistance and therefore a greater chance of fracturing rather than a pullout. However, flexural stiffness of the key is reduced in longer keys, and it is observed that the enclosing SHCC is cracking, thereby reducing the level of confinement and finally resulting in lower resistance. In addition, the tensile resistance of the key itself is governed by its fiber distribution. Likely, fibers are less favorably distributed in the geometry with the longest key. As a result, Geometry 3 (i.e. longest key) shows lower peak force compared to Geometry 2. This limitation is due to the experimental sample size, but by upscaling and creating larger elements, this issue might be resolved.

Geometry 3 showed a post-peak plateau in the force–displacement diagram (Fig. 9a). The plateau is likely a result of interfacial friction at the side of the key, which is the leading mechanism of force transfer once the adhesion between the two parts is lost.

In lubricated specimens, the trends are similar for different geometries (see Fig. 9b). The peak force is slightly higher when the geometry increases from 1 to 2 and 3. The same trend takes place for the displacement capacity that is clearly proportional to the length the key. The length of the post-peak plateau in this case is only dependent on the length of the keys (Fig. 9b), as lubrication minimizes the chemical adhesion between the two parts. Irrespective of their length, all lubricated keys could be fully pulled out without key failure (Fig. 11).

The averaged results of peak force and absorbed energy, which can be seen as key indicators of bond strength and ductility, are given in Fig. 12a for straight keys. Note that mean and standard deviation values are based on three tested samples (n = 3) per each geometry, as indicated in Fig. 3. The energy absorption capacity is calculated based on the final measured displacement, as the area
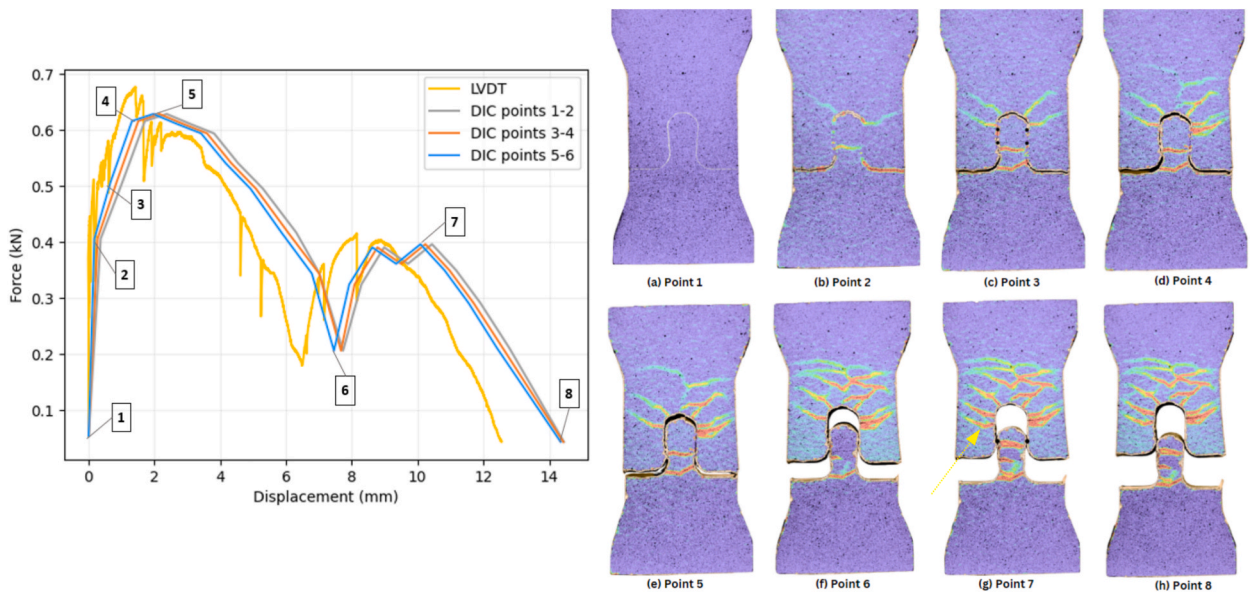
Fig. 16. (a) Load displacement curve from one of the tested specimens with lubricated interface and geometry 2 ($R_1/R_2 = 1.10$, CLG22) and (b) corresponding strain contours at different displacement levels.
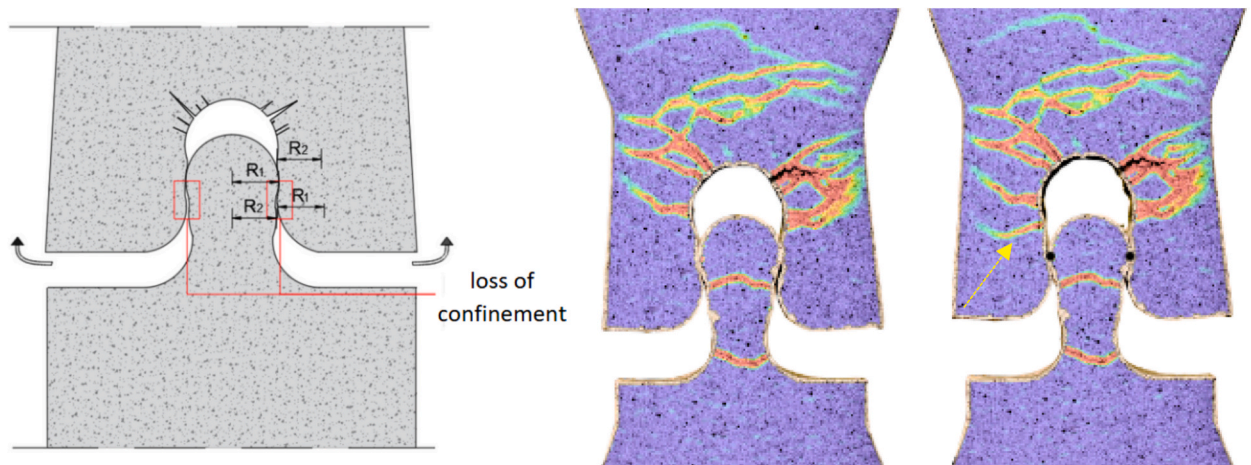
Fig. 17. (a) Schematic representation of the loss of confinement taking place after the second stable position in a bistable interlocked SHCC specimen, and (b) damage at the start and at the end of the second stable position in the lubricated sample with geometry 3 (CLG31) indicating with yellow arrow the crack that resulted in loss of confinement.

under force–displacement diagram. For untreated keys, the average peak force, although showing high scatter, is higher than that of the lubricated samples. On the other hand, the energy absorption is increasing as the key length increases, both for untreated and lubricated samples due to the friction. For lubricated keys, the peak force is relatively constant, and independent of the key length. This is in line with the previous numerical work [38], indicating that the depth of straight keys has limited influence on tensile strength but affects the post-peak behavior.

3.2.2. Bistable interlocking specimens

Varying radii ratios were examined to investigate the impact of the interface geometry on the tensile response of the curved keys. With untreated keys, different geometries show similar trends (Fig. 13a). All curves show similar peak force (around 1 kN), and a rather steep strain softening branch after the peak. Regarding displacement magnitude, untreated keys show a similar response which was not influenced by the key size. This was related to the fact that most keys failed (see Fig. 14); therefore, their displacement potential was not utilized. Some keys showed partial debonding (from one side), thus utilizing their ductility more efficiently, resulting in a gradual strain-softening regime.

With lubricated specimens, the bistable interlock mechanism was activated (Fig. 13b). Two peaks and two equilibrium positions
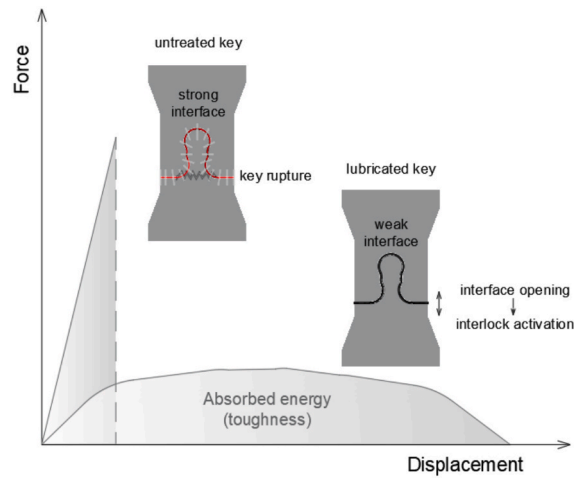
Fig. 18. Schematic representation of a strong (untreated) and weak (lubricated) interface in terms of energy absorption.

were observed, as documented in the bistable interlock literature [26,39]. Still, the second peak was for all geometries lower than the first peak, and the magnitude of the second peak was similar for all geometries. Geometries 2 and 3 with larger R_1/R_2 ratios resisted higher force compared to Geometry 1. The fracture behavior of lubricated samples (Fig. 15) was significantly different from that of untreated samples. Lubricated interfaces exhibited larger deformations and significantly more cracking, with radial cracks emanating from the interface region and propagating perpendicular to the interface. Finally, these cracks are either being locked within SHCC or reached the side surface of the specimen.

The detailed insight into damage development in one of the specimens (geometry 2) is shown in Fig. 16. In Fig. 16a, a comparison between the LVDT and the DIC measurement is shown, corresponding to a correlation coefficient (i.e., R^2 value) of around 0.7. Note however, that a direct comparison cannot be made in these tests due to an out-of-plane bending during a direct tensile test [40]. The applied DIC method has been extensively verified in our earlier studies in three point bending tests where control LVDTs were placed closer to the DIC measurement surface [30,41].

Initial cracking was observed within the key and starting from the interface and propagating further within SHCC. The load resistance kept increasing followed by more cracking within SHCC, also in the key. Once the first radius was pulled out, the load that could be resisted by the sample started decreasing. During this stage further cracking was formed. At point 6 the key was locked within the geometrical profile of the interface. This resulted in the load increase again, contributing to more cracks formed in the key and further slipping of the connection, finally reaching the second peak at Point 7. At this point, the side crack (labelled in yellow) was developed and the lateral confinement at the interface was lost. The load started decreasing again, finally leading to pullout of the key.

The details of confinement loss for Geometry 3 are shown in Fig. 17. The second stable position starts when interface slip reaches
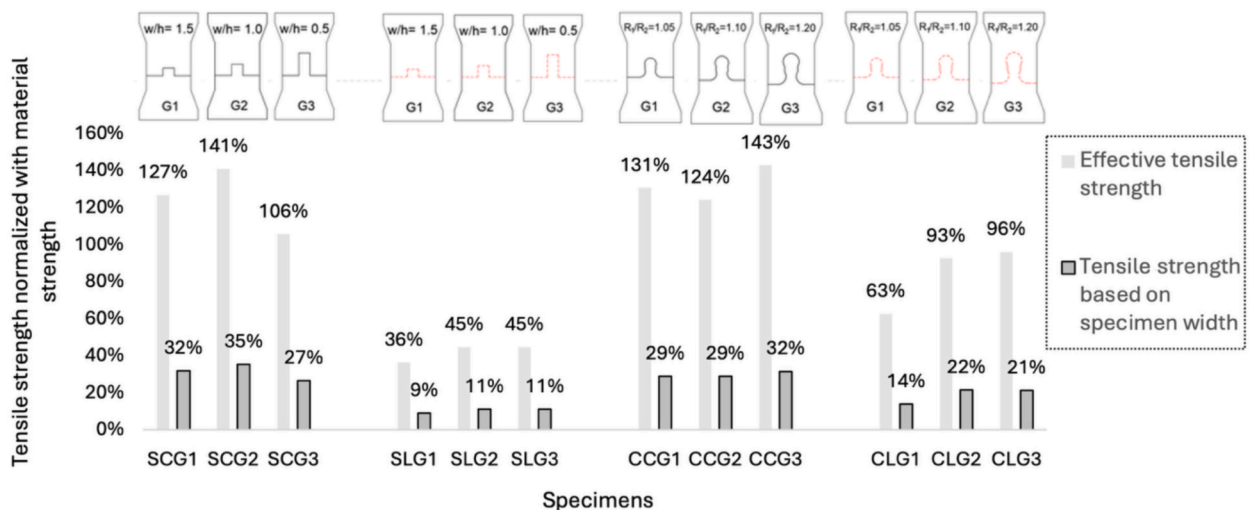

Fig. 19. Tensile strength of interface specimens based on the reduced cross-sectional area ("effective tensile strength") and the whole specimen width, compared to the obtained material strength of SHCC.
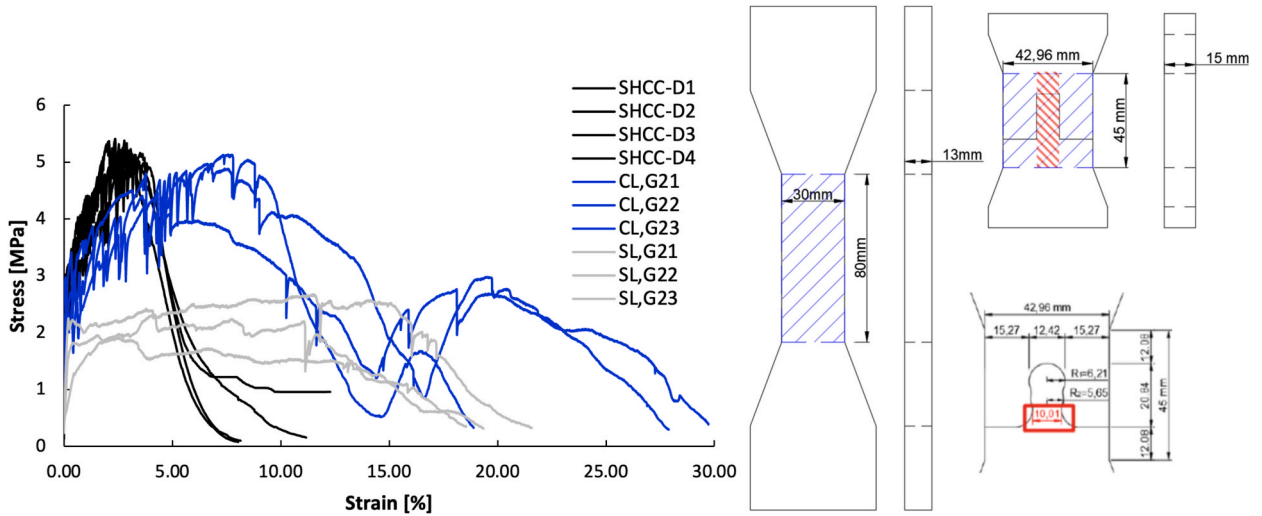
Fig. 20. (a) Relationship effective stress (=F/thickness/smallest key width, where the smallest width of the key is 10.8 mm for straight and 10.01 mm for curved Geometry 2) normalized strain (=Displacement/Length, where the Length is 80 mm for monolithic SHCC and 45 mm for interface specimens) of straight and curved keys (G2), with lubricated interfa compared to monolithic SHCC and (b) Gauge length in different specimens used for normalization.
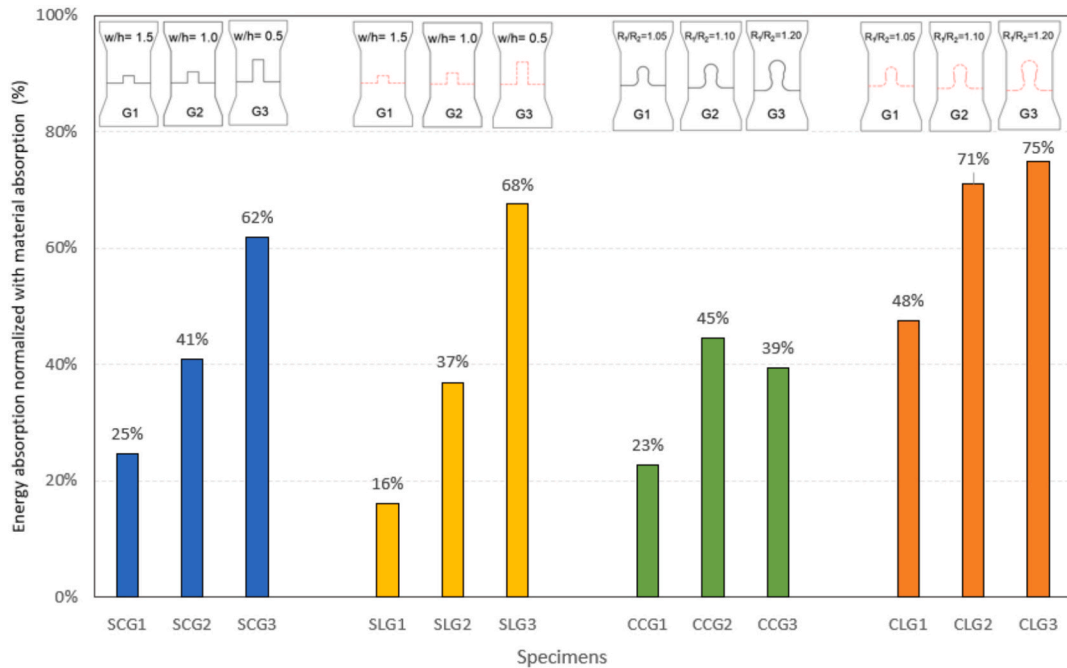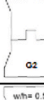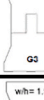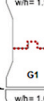

Fig. 21. Energy absorbed by SHCC specimens compared to the monolithic material's energy absorption.

the kink of the interface curve (Fig. 17a). This is when the bi-stable interlocking mechanism is activated. This location is dependent on the geometric characteristics of the system. The loss of confinement happens with the final lateral cracking (labelled with yellow arrow) leading to failure (Fig. 17b).

In the literature [26], bistable interlocking keys have previously been manufactured with ABS plastic. In the case of $R_1/R_2 = 1.05$, which corresponds to geometry 1 used herein, the bistable geometry subjected to monotonic pullout resulted in two peaks in the load–displacement curve (Fig. 1). However, while for ABS, the second peak was higher than the first one, with SHCC the second peak was lower. This is because ABS has a lower elastic modulus (around 1.5 GPa [42]), and the whole specimen could remain in the linear elastic regime during the pullout. Upon achieving the second equilibrium position, the elastic deformation had already been recovered. On the other hand, the elastic modulus of the used mix of SHCC is an order of magnitude higher (approximately 18 GPa [30]), and
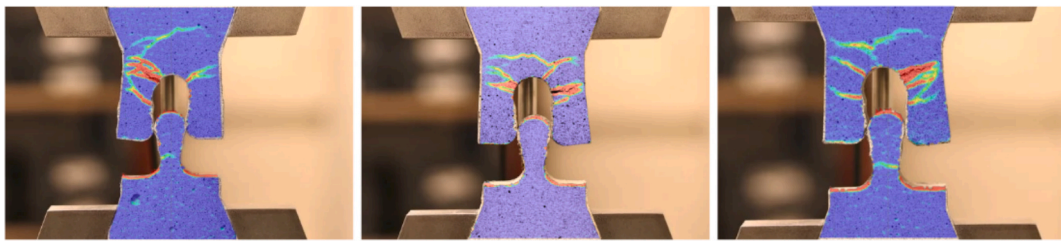
Table 4
Summary of all results and main features.

Specimen Type	Geometry	Notation	Peak force (kN)	Tensile Strength (MPa)			Effective tensile strength (MPa)			Absorbed energy (kN × mm)		
					Mean	STD		Mean	STD		Mean	STD
Straight non lubricated	w/h = 1.5	SCG1, 1	0.83	1.28			5.11			1.74		
		SCG1, 2	1.42	2.20	1.68	0.47	8.75	6.67	1.88	1.12	1.57	0.39
		SCG1, 3	1.00	1.55			6.16			1.85		
	w/h = 1.0	SCG2,1	0.89	1.38			5.51			1.43		
		SCG2,2	1.11	1.72	1.87	0.58	6.84	7.41	2.29	3.16	2.67	1.08
		SCG2,3	1.61	2.50			9.96			3.43		
	w/h = 0.5	SCG3,1	0.65	1.01			4.01			3.27		
		SCG3,2	0.99	1.54	1.39	0.33	6.12	5.53	1.32	6.45	4.06	2.11
		SCG3,3	1.04	1.62			6.45			2.46		
Straight lubricated	w/h = 1.5	SLG1, 1	0.37	0.58			2.30			1.66		
		SLG1, 2	0.25	0.38	0.48	0.10	1.53	1.92	0.39	0.83	1.11	0.48
		SLG1, 3	0.31	0.49			1.94			0.83		
	w/h = 1.0	SLG2,1	0.43	0.67			2.68			3.13		
		SLG2,2	0.39	0.61	0.59	0.10	2.42	2.34	0.39	2.34	2.45	0.64
		SLG2,3	0.31	0.48			1.91			1.87		
	w/h = 0.5	SLG3,1	0.45	0.70			2.79			5.31		
		SLG3,2	0.43	0.66	0.60	0.15	2.63	2.38	0.58	4.35	4.52	0.72
		SLG3,3	0.28	0.43			1.71			3.90		
Curved non lubricated	R1/R2 = 1.05	CCG1, 1	0.89	1.38			6.24			1.44		
		CCG1, 2	1.02	1.59	1.53	0.13	7.17	6.90	0.57	2.01	1.51	0.47
		CCG1, 3	1.04	1.61			7.28			1.07		
	R1/R2=1.10	CCG2,1	0.94	1.46			6.25			2.28		
		CCG2,2	1.14	1.76	1.51	0.23	7.57	6.50	0.98	3.91	2.96	0.85
		CCG2,3	0.85	1.32			5.67			2.69		
	R1/R2=1.20	CCG3,1	0.90	1.39			6.29			4.03		
		CCG3,2	1.17	1.81	1.66	0.24	8.21	7.52	1.07	1.74	2.61	1.24
		CCG3,3	1.15	1.78			8.07			2.06		
Curved lubricated	R1/R2 = 1.05	CLG1, 1	0.50	0.78			3.50			3.24		
		CLG1, 2	0.39	0.60	0.72	0.11	2.71	3.26	0.48	2.50	3.15	0.60
		CLG1, 3	0.51	0.79			3.59			3.69		
	R1/R2=1.10	CLG2,1	0.75	1.16			4.97			5.75		
		CLG2,2	0.68	1.05	1.14	0.08	4.51	4.87	0.32	4.88	4.51	1.45
		CLG2,3	0.77	1.20			5.13			2.91		
	R1/R2=1.20	CLG3,1	0.75	1.17			5.28			6.54		
		CLG3,2	0.75	1.17	1.11	0.10	5.30	5.02	0.47	5.30	4.96	1.77
		CLG3,3	0.64	0.99			4.48			3.04		
Curved prefab	R1/R2 = 1.20	CPG3, 1	0.50	0.78			3.54			4.25		
		CPG3, 2	0.43	0.66	0.68	0.09	2.99	3.08	0.43	3.39	3.56	0.62
		CPG3, 3	0.38	0.60			2.70			3.05		

(a)   *(b)*
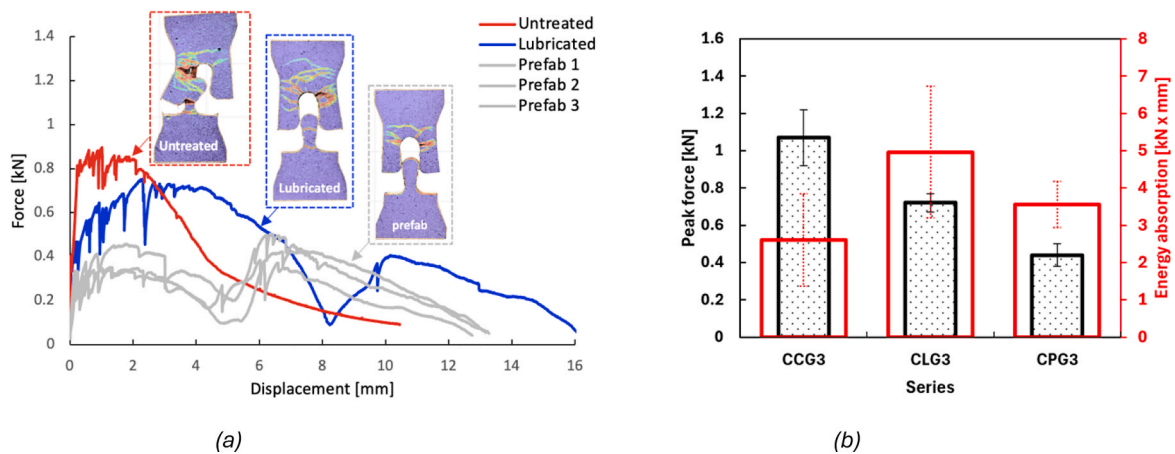
Fig. 22. (a) Force displacement relationship for curved keys (geometry 3) with untreated, lubricated, and assembled interface and (b) Average peak force and energy absorption for these samples.

Fig. 23. Failure modes of bistable interlocked specimens with assembled interface. Only geometry 3 was manufactured for this type of key.

cracking in the keys and SHCC (Fig. 15) resulted in irreversible deformation. Consequently, the second peak in Fig. 13b was always lower than the first peak.

The average peak force and absorbed energy are given in Fig. 12b for curved keys. With untreated keys, the peak force is relatively constant for different geometries, similarly as observed for straight profiles. In fact, geometry (straight vs. curved) did not induce statistically significant difference between the two groups, both with respect to the peak force (p = 0.65, n = 9) and absorbed energy (p = 0.53, n = 9). Untreated specimens show significantly higher peak force compared to lubricated samples (p-value < 0.0001, n = 18). For lubricated samples, curved keys show significantly higher peak force (p-value < 0.001, n = 9) and higher energy absorbed (with marginal evidence p = 0.05 of a difference) compared to straight samples.

For lubricated keys, the peak force increases significantly for increasing the R_1/R_2 ratio from geometry 1 to geometry 2 by 43.3 % (p = 0.0088, n = 3), whereas further increase in the R_1/R_2 ratio does not increase the peak force. Similar holds for energy absorption. This indicated a possible threshold over which the R_1/R_2 ratio increase does not bring additional benefits in strength and ductility. Overall, the energy absorption was significantly higher for lubricated compared to untreated curved keys. The untreated specimens created a stronger bond at the interface, making the two parts of the specimen behave like a monolithic material. On the other hand, lubricated specimens with a weak interface can utilize friction and interlock to delay strain localization and absorb a significant amount of energy before failure, leading also to a smaller scatter, both in strength and energy absorption. This mechanism is schematically shown in Fig. 18.

Fig. 19 shows the strength of tested SHCC-SHCC interfaces relative to SHCC material tensile strength. The strength is normalized for the whole width of the specimen (as indicated in Fig. 20b in blue), and for the reduced cross sectional area (i.e. width of the key only, Fig. 20b in red) and defined as "effective tensile strength". In a real connection, the keys would repeat in such a way that the total

Table 5
Peak force (F_2/F_1) ratio in lubricated and "pre-fabricated" keys. Standard deviation is indicated.

Series	F_2/F_1 (average)
CLG1	0.89 ± 0.05
CLG2	0.52 ± 0.17
CLG3	0.38 ± 0.16
CPG3	1.14 ± 0.11

frequency of keys is identical to the width of the tested specimen, so the stress normalized to the specimen width assess the efficiency of the connection. With the plot on "effective tensile strength", a more local phenomenon is investigated, as the load in specimens is transferred through keys only, so the local stress inside the key is governing. This stress is relatively high and sometimes even higher than the SHCC material strength (e.g. for untreated specimens), likely due to specific confining conditions.

The specimens with the highest strength are the straight and curved keys with an untreated interface (SC, CC). Most specimens in these cases failed due to a key failure. The strength of the lubricated specimens was significantly lower, but all specimens showed full or partial pull-out failure of the key.

Although the interface is weaker compared to the monolithic SHCC specimen, a higher strain capacity compared to monolithic SHCC is observed (Fig. 20a). This ductility is activated by controlled tightly spaced microcracks in the key and microcracks in the surrounding material, in direction perpendicular to the interface surface. Significantly higher effective stress was resisted by curved compared to straight samples. In addition, the effective tensile strength of curved lubricated specimens is almost reaching the strength of SHCC.

In Fig. 21, an absolute comparison of the energy absorbed for all the specimens compared to the SHCC energy absorption is shown. Due to the difference in cross-section and heights between specimens, energy was normalized, with the gauge height and the whole cross-sectional area of each specimen (as seen in Fig. 20b). The energy values were calculated per cubic millimeter (Joules/mm^3). Some specimens can reach 62–75 % of the SHCC energy absorption. The geometrical hardening effect, along with the multiple microcracking behavior of SHCC (strain hardening), allowed that the small area of the key (i.e. approximately 10–25 % of specimen width) across 50 % of specimen gauge length absorb energy comparable to the bulk material.

An overview of all results and main features is given in Table 4.

3.2.3. Assembled (prefab) bistable interlocking specimens

The force/displacement graphs and the DIC results of the assembled (prefab, demountable) specimens are shown in Fig. 22a and Fig. 23, respectively. The results can also be compared to untreated and lubricated specimens of the same geometry (Fig. 22a). Interestingly, the second peak in the bistable interlocking curve is higher than the first peak. As shown in the literature [25,39], this feature can enhance the overall mechanical stability of the system. Furthermore, in structural applications, this can be exploited as a safety mechanism: once the first equilibrium position has been passed, one can rely on the second equilibrium position with a higher load-bearing capacity.

The ratio of second peak to first peak force (F_2/F_1) for all specimens with the same geometry (i.e., including untreated, lubricated, and prefabricated keys) is given in Table 5, and is higher in assembled compared to lubricated keys. Peak force and energy absorption of all samples with the same geometry is given in Fig. 22b. The prefabricated connection showed the lowest peak force, and the lubricated key showed the highest energy absorbed.

For the prefab connection, *a higher F_2/F_1* is observed likely because of the assembly gap that provides more relative displacement in the connection. More specifically, compared to the same geometry with a cast connection (both untreated and lubricated), a larger gap between two parts in prefabricated connection reduces F_1 since a lower force is required to pass the first stable position. On the other hand, F_2 is related to the plasticity of SHCC in the second stable position. Due to low friction, both the lubricated and the prefab sample exhibit distinct F_2 with similar values. Assembly gap and lower friction ensure that prefab samples exhibit less cracking and smaller deformation capacity compared to lubricated samples.

Compared to traditional concrete-concrete connections, the proposed bi-stable connection relies on the geometry, rather than (solely) on the material properties. The ductility of the connection can be engineered (i.e., tailored) as needed, much beyond that offered by any cementitious material (including SHCC) by changing the geometry of the keys. In addition, the movement should be reversible, unlike (partly) irreversible plastic damage that would occur in SHCC under high strain. Furthermore, the interlocking will (ideally) provide two discrete equilibrium positions under tensile loading. If a connection would move from equilibrium 1 to equilibrium 2, this would provide a simple measure of the loading state of the connection. For this concept to be practical, an automated monitoring approach would need to be integrated into the connection.

The bistable interlocked specimens with lubricated interfaces, or prefabricated, failed in a pull-out mode with socket side opening, allowing high toughness, unlike specimens with untreated interfaces exhibiting key fracture. However, the specimen width is relatively small, resulting in limited lateral confinement. In real structures, such as bridge shear keys, or with multiple keys placed along a wider interface, the lateral confinement is higher. This increased confinement could influence the failure mode and ductility behavior, potentially favoring key fracture over interface slip, and finally resulting in lower ductility. This limitation will affect the applicability of the current findings to full-scale structures with multiple keys placed along which might require a modified interface design to be tailored accordingly.

4. Conclusions

The tensile performance of interface interlock geometries combined with ductility of SHCC are investigated with a goal to increase toughness of intrinsically brittle concrete-to-concrete interface. Based on the performed research, the following major conclusions can be drawn:

- Observed failure modes include fracture and/or pullout of the key, combined with the varying extent of SHCC microcracking, distributed mainly perpendicular to the interface geometry. Unlike in polymers where the interlocking mechanism relies on elastic

deformation of tabs, in this research, the toughness increase is mainly governed by the extent of SHCC microcracking activated around the interface and quasi-plastic deformation of the tabs.

- Reling on the principle of segmentation and frictional interfaces to increase toughness and flexibility, trade is made by losing strength and stiffness, similar as observed in polymer structures.
- The strength of the connection is around 30 % of the SHCC material strength, when normalized to the whole cross-sectional area, and up to 97 % when normalized to the (smallest) width of the key, whereas the strain capacity of the connection can exceed the strain capacity of monolithic SHCC. To account for strength loss, possibly use of high-strength SHCC and ultra-high performance concrete to facilitate demountable connection with sufficient load carrying capacity can be designed.
- The tensile response (regarding strength and toughness) of the interlocking keys under tensile loading is highly influenced by the geometry of the key (i.e. straight or curved) and interface conditions (i.e. untreated or lubricated specimens). With untreated keys, straight or curved, a large percentage of the specimens failed due to the key failure. As a result, in terms of strength, there were no benefits observed from changing the interface geometry from straight to curved. For the lubricated keys, most specimens showed a full pull-out failure of the key, whereas changing the geometry from straight to bistable interlocked added benefits regarding the peak force and energy absorbed.
- The adhesive bonding at the interface in the untreated interface did not improve the toughness of the connection. An interface with a lower bond strength is beneficial for ductility, as it was with curved keys, where lubrication enabled more microcracking and higher exploitation of the geometrical interlock. Change of the geometry (larger length of key or radii ratio) also improved the peak strength and energy absorbed. For the straight keys, a proportional increase in absorbed energy was noticed for untreated and lubricated specimens, but not in strength. For the untreated curved specimens, the increase in geometry yielded no major differences since the key failure governed the response.
- The prefabricated key, while not showing outstanding peak force or ductility in comparison to the other series of specimens, had manufacturing benefits and offered extra mechanical stability in terms of the second equilibrium position. Furthermore, with manufacturing tolerances between the two assembled parts, the probability of key failure is lower than in other considered cases. In addition, the fabrication process could be easier to implement in many practical cases.

The present study shows the potential of using engineered interfaces, in this case, bistable interlocks, in concrete-to-concrete connections. The efficiency of the connection depends on the material, geometry, and fabrication methods. Note that, herein only a relatively simple case of uniaxial tensile loading was considered. Further research should explore interface performance under more complex stress states (e.g. shear, combined compression-shear loading) which are closer to practical service conditions. Furthermore, the increased confinement in actual structures might influence the failure mode and ductility behavior, potentially favoring key fracture over interface slip, thereby reducing the ductility. This will affect the applicability of the current findings to full-scale structures which might require a modified interface design. Finally, there might be potential practical challenges, related to costs, scalability and constructability, of proposed methods (e.g. 3D-printed molds, interface lubrication) in real-world engineering structures. These aspects will be a focus of our future research. The final goal is to design reliable and durable connections in concrete structures with high damage tolerance.

CRediT authorship contribution statement

Sofia Papoulidou: Writing – original draft, Investigation, Formal analysis, Data curation, Conceptualization. **Shan He:** Supervision, Methodology, Conceptualization. **Branko Šavija:** Writing – review & editing, Supervision, Methodology, Funding acquisition, Conceptualization. **Mladena Luković:** Writing – review & editing, Supervision, Funding acquisition, Conceptualization.

Declaration of competing interest

The authors declare that they have no known competing financial interests or personal relationships that could have appeared to influence the work reported in this paper.

Acknowledgment

Data availability

Data will be made available on request.

References

[1] Bentz E, Foster S, Fernández Ruiz M, Muttoni A, Sigrist V, Walraven J. Fédération Internationale du Béton (fib). Model Code 2010. 2010-first complete draft, chapters 7.3 and 7.13. Fédération Internationale du Béton, Bulletin 56.

[2] Randl N. Design recommendations for interface shear transfer in fib Model Code 2010. Struct Concr 2013;14(3):230–41.

[3] Daneshvar D, Behnood A, Robisson A. Interfacial bond in concrete-to-concrete composites: a review. Constr Build Mater 2022;359:129195.

[4] Lukovic M, Ye G. Effect of moisture exchange on interface formation in the repair system studied by X-ray absorption. Materials 2015;9(1):2.

[5] Lukovic M, Schlangen E, Ye G, Van Breugel K. Moisture movement in cement-based repair systems monitored by X-ray absorption. Heron 2017;62:21.

[6] Silfwerbrand J, Beushausen H, and Courard L. (2011). Bond. Bonded Cement-Based Material Overlays for the Repair, the Lining or the Strengthening of Slabs or Pavements: State-of-the-Art Report of the RILEM Technical Committee 193-RLS: 51-79.

[7] Lukovic M. (2016). Influence of interface and strain hardening cementitious composite (SHCC) properties on the performance of concrete repairs. In: TU Delft, Delft University of Technology.

[8] Santos DS, Santos PM, Dias-da-Costa D. Effect of surface preparation and bonding agent on the concrete-to-concrete interface strength. Constr Build Mater 2012; 37:102–10.

[9] Lukovic M, Schlangen E, Ye G, and van Breugel K. (2016). Moisture exchange in concrete repair system captured by X-ray absorption. ICCRRR 2015: 4th international conference on concrete repair, rehabilitation and retrofitting.

[10] Garbacz A, Courard L, Kostana K. Characterization of concrete surface roughness and its relation to adhesion in repair systems. Mater Charact 2006;56(4–5): 281–9.

[11] Courard L. Parametric study for the creation of the interface between concrete and repair products. Mater Struct 2000;33(1):65–72.

[12] Wang P, Jiao M, Hu C, Tian L, Zhao T, Lei D, et al. Research on bonding and shrinkage properties of SHCC-repaired concrete beams. Materials 2020;13(7):1757.

[13] He S, Nuri M, Jonkers HM, Luković M, Schlangen E. Structural behaviour of reinforced concrete beams with self-healing cover zone as lost formwork. Dev Built Environ 2024;18:100458.

[14] Beushausen H, Alexander M. Bond strength development between concretes of different ages. Mag Concr Res 2008;60(1):65–74.

[15] Martinola G, Sadouki H, Wittmann F. Numerical Model for Minimizing the risk of damage in a Repair System. J Mater Civ Engng 2001;13(2):121–9.

[16] Lukovic M, Šavija B, Schlangen E, Ye G. A Modelling Study of Drying Shrinkage damage in Concrete Repair Systems. Structural Faults & Repair 2014.

[17] Lukovic M, Schlangen E, Ye G, and Šavija B. (2013, 11-14 March 2013). Impact of surface roughness on the debonding mechanism in concrete repairs. Proceedings of the 8th International Conference on Fracture Mechanics of Concrete and Concrete Structures (FraMCoS-8), Toledo, Spain.

[18] Zareiyan B, Khoshnevis B. Effects of interlocking on interlayer adhesion and strength of structures in 3D printing of concrete. Autom Constr 2017;83:212–21.

[19] Wang L, Liu Y, Yang Y, Li Y, Bai M. Bonding performance of 3D printing concrete with self-locking interfaces exposed to compression–shear and compression–splitting stresses. Addit Manuf 2021;42:101992.

[20] Zhou W, McGee W, Gökçe HS, Li VC. A bio-inspired solution to alleviate anisotropy of 3D printed engineered cementitious composites (3DP-ECC): Knitting/ tilting filaments. Autom Constr 2023;155:105051.

[21] Dyskin AV, Estrin Y, Pasternak E, Khor HC, Kanel-Belov AJ. Fracture resistant structures based on topological interlocking with non-planar contacts. Adv Engng Mater 2003;5(3):116–9.

[22] Mirkhalaf M, Zreiqat H. Fabrication and Mechanics of Bioinspired Materials with Dense Architectures: Current Status and Future Perspectives. JOM: The Journal of The Minerals, Metals & Materials Society (TMS) 2020;72(4).

[23] Mirkhalaf M, Sunesara A, Ashrafi B, Barthelat F. Toughness by segmentation: Fabrication, testing and micromechanics of architectured ceramic panels for impact applications. Int J Solids Struct 2019;158:52–65.

[24] Molotnikov A, Gerbrand R, Qi Y, Simon GP, Estrin Y. Design of responsive materials using topologically interlocked elements. Smart Mater Struct 2015;24(2): 025034.

[25] Malik IA, Mirkhalaf M, Barthelat F. Bio-inspired "jigsaw"-like interlocking sutures: Modeling, optimization, 3D printing and testing. J Mech Phys Solids 2017; 102:224–38.

[26] Mirkhalaf M, Barthelat F. Design, 3D printing and testing of architectured materials with bistable interlocks. Extreme Mech Lett 2017;11:1–7.

[27] Li VC. On engineered cementitious composites (ECC). J Adv Concr Technol 2003;1(3):215–30.

[28] Luković M, Dong H, Šavija B, Schlangen E, Ye G, Kv B. Tailoring strain-hardening cementitious composite repair systems through numerical experimentation. Cem Concr Compos 2014.

[29] Van Zijl G and Stander H. (2008). SHCC repair overlays for RC: Interfacial bond characterization and modelling.

[30] Mustafa S, Singh S, Hordijk D, Schlangen E, Luković M. Experimental and numerical investigation on the role of interface for crack-width control of hybrid SHCC concrete beams. Engng Struct 2022;251:113378.

[31] Jun P, Mechtcherine V. Behaviour of strain-hardening cement-based composites (SHCC) under monotonic and cyclic tensile loading: part 1–experimental investigations. Cem Concr Compos 2010;32(10):801–9.

[32] Li VC. On engineered cementitious composites (ECC) a review of the material and its applications. J Adv Concr Technol 2003;1(3):215–30.

[33] Zhou J, Qian S, Sierra Beltran MG, Ye G, van Breugel K, Li VC. Development of engineered cementitious composites with limestone powder and blast furnace slag. Mater Struct 2010;43:803–14.

[34] He S, Zhang S, Luković M, Schlangen E. Effects of bacteria-embedded polylactic acid (PLA) capsules on fracture properties of strain hardening cementitious composite (SHCC). Engng Fract Mech 2022;268:108480.

[35] NEN-EN. European Committee for Standardization NEN-EN 197-1: Cement - Part 1: Composition, specifications and conformity criteria for common cements. In.

[36] Roux S, Réthoré J, Hild F. Digital image correlation and fracture: an advanced technique for estimating stress intensity factors of 2D and 3D cracks. J Phys D Appl Phys 2009;42(21):214004.

[37] McCormick N and Lord J. (2010). Digital image correlation. Materials today 13(12): 52-54.

[38] Lukovic M, Schlangen E, Ye G, and Savija B. (2013). Impact of surface roughness on the debonding mechanism in concrete repairs. Proceedings of the 8th International Conference on Fracture Mechanics of Concrete and Concrete Structures, Toledo, Spain.

[39] Hu W, Mengzhu Y, Yufan W. Closed-loop optimization and investigation of bistable interlocked structure. Int J Mech Sci 2018;144:10–23.

[40] Hordijk DA. Local approach to fatigue of concrete, Ph. D thesis. TU Delft 1991.

[41] Luković M, et al. Strain Hardening Cementitious Composite (SHCC) for crack width control in reinforced concrete beams. Heron 2019;64(1/2):181.

[42] Xu Y, Šavija B. Development of strain hardening cementitious composite (SHCC) reinforced with 3D printed polymeric reinforcement: Mechanical properties. Compos B Engng 2019;174:107011.